JOURNAL OF SYNCHROTRON RADIATION
ISSN 1600-5775

3D digital anatomic angioarchitecture of the mouse brain using synchrotron-radiation-based propagation phase-contrast imaging

Shupeng Shi,[a,b] Haoran Zhang,[a,b] Xianzhen Yin,[c] Zhuolu Wang,[d] Bin Tang,[a,b] Yuebei Luo,[a,b] Hui Ding,[a,b] Zhuohui Chen,[a,b] Yong Cao,[e] Tiantian Wang,[a,b] Bo Xiao[a,b] and Mengqi Zhang[a,b]*

[a]Department of Neurology, Xiangya Hospital, Central South University, 87 Xiangya Road, Changsha, Hunan 410008, People's Republic of China, [b]National Clinical Research Center for Geriatric Disorders, Xiangya Hospital, Central South University, Changsha, Hunan 410008, People's Republic of China, [c]Center for Drug Delivery System, Shanghai Institute of Materia Medica, Chinese Academy of Sciences, Shanghai 201203, People's Republic of China, [d]Department of Breast Surgery, Hunan Provincial Maternal and Child Health Care Hospital, Changsha, Hunan 410008, People's Republic of China, and [e]Department of Spine Surgery, Xiangya Hospital, Central South University, Changsha 410008, People's Republic of China. *Correspondence e-mail: zhangmengqi8912@163.com

Received 10 October 2018
Accepted 10 May 2019

Edited by S. M. Heald, Argonne National Laboratory, USA

Keywords: high resolution; mouse brain; angioarchitecture; propagation phase-contrast imaging.

Thorough investigation of the three-dimensional (3D) configuration of the vasculature of mouse brain remains technologically difficult because of its complex anatomical structure. In this study, a systematic analysis is developed to visualize the 3D angioarchitecture of mouse brain at ultrahigh resolution using synchrotron-radiation-based propagation phase-contrast imaging. This method provides detailed restoration of the intricate brain microvascular network in a precise 3D manner. In addition to depicting the delicate 3D arrangements of the vascular network, 3D virtual micro-endoscopy is also innovatively performed to visualize randomly a selected vessel within the brain for both external 3D micro-imaging and endoscopic visualization of any targeted microvessels, which improves the understanding of the intrinsic properties of the mouse brain angioarchitecture. Based on these data, hierarchical visualization has been established and a systematic assessment on the 3D configuration of the mouse brain microvascular network has been achieved at high resolution which will aid in advancing the understanding of the role of vasculature in the perspective of structure and function in depth. This holds great promise for wider application in various models of neurovascular diseases.

1. Introduction

The spatial configuration of mammalian brain microvasculature is a great challenge in view of its exquisite and intricate three-dimensional (3D) structure. The vascular networks are crucial to provide nutrition for tissues (Heinke *et al.*, 2012). The vasculature is essential for maintaining normal brain function by means of efficient transportation of oxygen and nutrient substances (Heinke *et al.*, 2012; Solis Jr *et al.*, 2018). There are a wide variety of neurovascular diseases resulting from vascular malfunctions (Mazzetti *et al.*, 2004). Microvascular alterations appear early in neurological disorders. Visualization of the brain spatial angioarchitecture is therefore the key element to directly identify the vascular changes during diverse pathological courses (Zhang *et al.*, 2015; Wu *et al.*, 2018). Additionally, a precise depiction of the distribution of the blood supply gives deep insight into advancing our understanding of neurovascular function and facilitates the development of effective therapeutic strategies (Hu *et al.*, 2015). Histological studies are commonly employed for two-dimensional (2D) standard analysis of biological

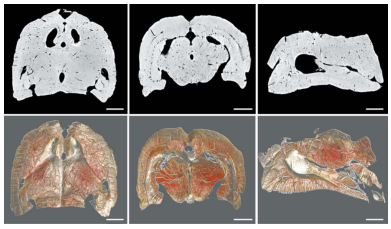

specimens, which are incapable of demonstrating the authentic spatial structure of vascular networks (Zhang *et al.*, 2015). Scanning electron microscopy by casting perfusion method is a useful tool for visualization of the 3D microvascular networks (Wu *et al.*, 2018). However, these complicated procedures and invasive perfusion of casting agents compromise sample integrity (Lazzari & Franceschini, 2000). Whereas two-photon laser scanning has the capability for vessel visualizing in 3D on the high-resolution scale, the low tissue penetration depth limits their use (Lindvere *et al.*, 2010).

To overcome these deficiencies, radiographic imaging has been proposed as a nondestructive tool to visualize the structure of vessels (Heinzer *et al.*, 2006; Kline *et al.*, 2010). Conventional X-ray computed tomography (CT) serves as attenuation-based X-ray imaging, which is disenable to image weak X-ray absorption biological soft tissues like tumors and vessels without angiography and insufficiently reliable to provide high resolution and exquisite structure of the integral vasculature (Hu *et al.*, 2014; Zhang *et al.*, 2014*a*,*b*). To address these issues, it is desirable to establish a novel imaging technique to present the complicated 3D angioarchitecture of the brain in a panoramic view.

Recently, state-of-the-art synchrotron radiation (SR) X-ray sources have been applied in medical research. Such sources are capable of high-resolution imaging of thick tissues, achieving high directionality with sufficient photon flux, monochromatization and small divergence (Zhang *et al.*, 2014*a*,*b*; Carlton *et al.*, 2016; Giuliani *et al.*, 2017; Hu *et al.*, 2017). Currently, SR-based phase-contrast imaging (PCI) utilizes X-ray phase shift, which is approximately 1000 times more sensitive to refractive index information than conventional X-ray absorption imaging, and is especially appropriate for 3D characterization of delicate microstructures in biological samples with low X-ray absorption without the aid of contrast agents (Zhang *et al.*, 2014*a*,*b*, 2015; Bravin *et al.*, 2013). At least five types of technique are available in PCI, including propagation phase-contrast imaging (PPCI), analyzer-based imaging, crystal interferometry, and grating interferometric and grating non-interferometric methods (Zhang *et al.*, 2014*a*; Bravin *et al.*, 2013; Zhou & Brahme, 2008). In particular, PPCI is the simplest PCI without the requirements of complex optical devices in the light path, which permits coherent X-rays propagating from the sample to produce detectable phase shifts and convert to different signal intensities (Bravin *et al.*, 2013; Zhou & Brahme, 2008); Liao *et al.*, 2017). This method has proven to be an excellent tool for 3D visualization of soft tissues such as tumors, microvessels and neurons *ex vivo* (Zhang *et al.*, 2014*a*, 2015; Wu *et al.*, 2018). Recent studies have verified that SR-PCI allows the 3D visualization and quantitative analysis of the neuronal-network in *ex vivo* mouse spinal cord on the submicrometre scale (Bukreeva *et al.*, 2017), even simultaneous observation of 3D micro-vascular networks and neuronal systems without aggressive sample preparation or sectioning (Fratini *et al.*, 2015). In a multiple sclerosis mouse model, Cedola used this technique to obtain unprecedented direct 3D simultaneous imaging of neurovascular networks of lesions at the micro- to nanoscale (Cedola *et al.*, 2017). Moreover, their team utilized PCI to visualize the internal structure of Aβ plaques and disease-relevant vascular and neuronal networks in Alzheimer's disease mouse brain at the capillary level in detail without sectioning and staining (Lorenzo *et al.*, 2019).

In the current study, we aimed to explore the potential SR-based PPCI for visualization of the global angioarchitecture from 2D to 3D in mouse brain. We also attempted to perform virtual micro-endoscopy of brain vessels to dynamically track targeted vessels from the luminal side. This new technique enables us to navigate through relevant blood vessels in a non-invasive manner to identify pathological changes of inner vascular endothelium in neurovascular diseases. It is also able to visualize randomly selected vessels within the brain, which will assist clarification of the intricate angioarchitecture. Based on our data, we propose an approach which establishes systematic visualization on the hierarchical vascular imaging of the mouse brain, which may serve as a promising tool for pre-clinical research on vascular pathologies, particularly in the explorations of interactions between vascular and neural networks.

2. Methods

2.1. Experimental animals and ethics statement

A total of ten male C57BL/6 (body weight 25–35 g) mice were obtained from the Animal Center of Central South University (Changsha, China) and were kept in a temperature-controlled room with a 12 h light/dark cycle with free access to food and water. They were randomly divided into two groups (*A* and *B*, $n = 5$ each). The samples from group *A* were scanned by PPCI and those from group *B* were prepared for histological observation. The animal care and use was performed in accordance with the guidelines established by the Animal Care and Use Committee of the Central South University. The protocol was approved by the Committee on the Ethics of Animal Experiments of Central South University.

2.2. Sample preparation

After the mice were deeply anesthetized, thoracotomy was rapidly performed to expose the heart. Heparinized saline was rapidly infused into the circulatory system via the ascending aorta, allowing an effective drain of blood flow. Ten percent buffered formalin was transcardially perfused for tissue fixation. All the perfused solutions were preheated to 37°C, and the procedure was conducted in a laboratory at 22°C. Mice brains were then extracted and post-fixed at 4°C for 24 h with 10% buffered formalin solution. The specimens in group *A* were subsequently rinsed and dehydrated with a gradient of ethyl alcohol for 24 h each, and were finally dried in air in a fully dehydrated state before PPCI scanning.

2.3. PPCI scanning and image processing

The specimens were scanned using PPCI performed at the BL13W1 beamline of the Shanghai Synchrotron Radiation

Facility (SSRF, China). The SR X-rays were generated from an electron storage ring with an accelerated energy of 3.5 GeV and an average beam current of 200 mA. The beamline covered a tunable energy spectrum ranging from 8 to 72.5 keV. After being monochromated with a double-crystal monochromator, the transmitted SR was captured by a 100 µm-thick cleaved single-crystal $CdWO_4$ scintillator, and converted to a visible image detected by a 3.7 µm pixel^{-1} CCD camera (Photonic Science, UK). The sample was fixed on the rotary stage, which was exposed to the SR light path, and the distance between the sample stage and the detector could be adjusted in the range 0–8 m. To obtain better X-ray phase-contrast images, the monochromatic X-ray energy was adjusted to 20 keV, the exposure time was set to 1.5 s, and the sample-to-detector distance (SDD) was adjusted to 50 cm. While the sample stage rotated by 180°, a total of 900 initial projections were captured. Additionally, ten light-field images and five dark-field images were recorded during image acquisition, to eliminate background noise and variations in the brightness of the X-ray source. After scanning, all projections were transformed into 2D slice sections using the *Phase-sensitive X-ray Image processing and Tomography REconstruction* (*PITRE*) software (applied by the BL13W1 experimental station). *PITRE* supports phase retrieval for propagation-based phase-contrast imaging/tomography (PPCI/PPCT) and allows parallel-beam tomography reconstruction for PPCT data (Chen *et al.*, 2012). For the principle of phase-contrast imaging, the interaction between waves and objects influences the amplitude and phase of the X-rays, and the refractive index n of the medium ($n = 1 - \delta + i\beta$) can represent the forward diffraction. Here, δ is the refractive index decrement in relation to the phase shift, and the absorption index β refers to the linear absorption coefficient. Then phase retrieval was used for the individual projections to convert the phase-contrast fringes into phase-based area contrast, according to an estimate of the phase-attenuation ratio (parameter of δ/β), which was based on a 'single distance' phase-retrieval algorithm by Paganin *et al.* (2002). Regarding the phase extraction, the parameter δ/β was adjusted to 100 on the basis of a preliminary experiment. The reformatted digital slice images were generated using fast slice reconstruction software based on the fast Fourier transformation algorithm (supplied in *PITRE* by BL13W1) with a high-quality phase contrast. Via 2D slices, microvessels in the scanned sample could be distinguished within the parenchyma.

2.4. 3D visualization of angioarchitecture

A series of 2D slices were reconstructed using *Image Pro Analyser 3D* software (Version 7.0, Media Cybernetics, Inc., USA), *VG Studio Max* (Version 3.0, Volume Graphics GmbH, Germany) and *Amira* (Version 6.0.1, Mercury, Richmond, TX, USA) to generate the 3D images. After the vasculature was segmented from the brain parenchyma with *Image Pro Analyser 3D* based on the iterative gray level threshold algorithm, we established a 3D vessel tree skeleton model for vascular structure characterization to extract the centerline of the vessel trees.

2.5. Histological observation

For histological observation, the samples from group *B* were post-fixed in 4% paraformaldehyde in PBS overnight, followed by cryoprotection with 30% sucrose/PBS overnight, and embedding in an optimal cutting temperature compound (Sakura Finetek USA) for 10 µm-thick sections. They were proceeded to hematoxylin and eosin (HE) staining for histological observation. Images were captured by optical microscope (Leica DM4000B, Germany) and compared with 3D images by PPCI.

2.6. 3D pseudo-color connectivity map of focal angioarchitecture

In order to visualize the microvasculature in detail, high-resolution images of focal vascular trees obtained from SR-based PPCI were rendered by coding each vessel branch base on their connectivity with diverse distinct colors, allowing reading out of the vessel distribution directly within the targeted brain region.

2.7. 3D virtual micro-endoscopy

After the 3D rendering model generated by the constructor module plug in *Image Pro Analyzer 3D*, the virtual reality modeling endoscopic images of the brain microvasculature could be exported. With the manipulation of the software, a 'realistic virtual 3D flight' navigation along the vessel path could be performed.

2.8. Immunohistochemistry

The samples were sectioned as described above for histological observation. Coronal sections were collected and washed three times with PBS. Antigen unmasking was performed for CD31 using a PBS solution with 1 µg ml^{-1} proteinase K (15 min at room temperature). Sections were then blocked by PBS with 0.25% triton and 20% normal horse serum (90 min at 22°C). Samples were then incubated overnight at 4°C with a primary antibody, anti-CD31 (1:100; Abcam, Cambridge, UK). After that, samples were incubated with horseradish peroxidase-conjugated secondary antibody (1:200 dilution; Santa Cruz Biotechnology, Santa Cruz, CA, USA) for 1 h at 22°C. Samples were then stained by both the diaminobenzidine kit (Maixin, Fuzhou, China) and Harris hematoxylin. Photographs were taken using an Olympus BX51 microscope (Olympus, Tokyo, Japan).

3. Results

3.1. SR-PPCI projection of cerebral vessels in normal mice

The 3.7 µm CCD detector was able to capture rich internal details to ensure the integrity of the field of view and the clarity of the imaging. The original projection (Fig. 1) covered the whole brain and clearly showed vessels with various

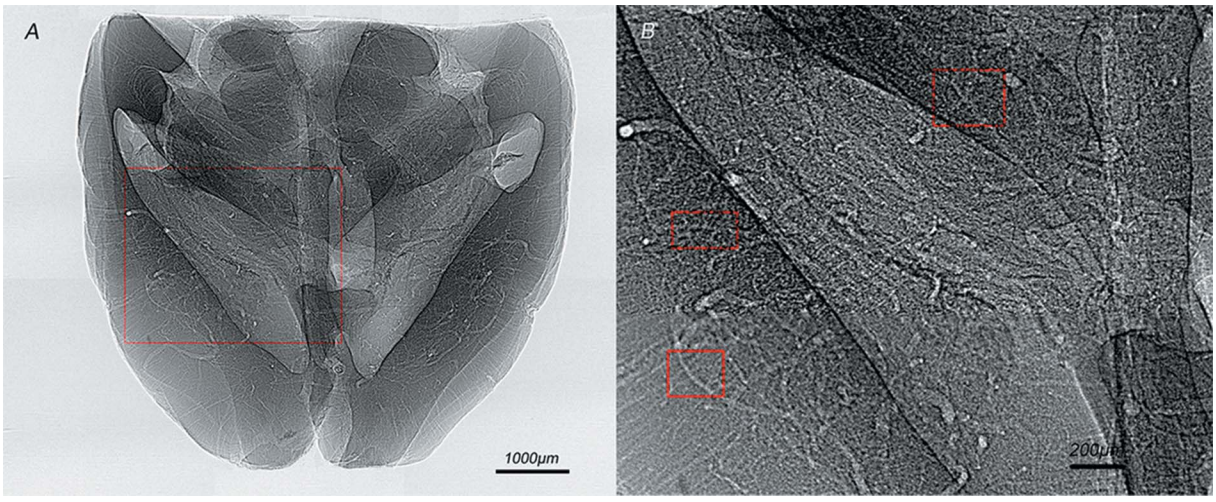

Figure 1
(A) Synchrotron radiation in-line PCI projection of cerebral vessels in normal mice obtained using a 3.7 μm CCD. (B) Local magnification of the region of interest denoted by the red frame in (A). The small red box in (B) indicates vessels with diameter of approximately 10 μm.

diameters in the brain. In the absence of contrast agents, microvessels approximately 10 μm wide could be discriminated. The images showed that well arranged cortical vessels wriggled naturally and the deep perforators could be clearly discerned.

3.2. Micro-tomography of 3D brain angioarchitecture

We obtained detailed cerebral 3D digitalized angioarchitectural maps (Fig. 2). Herein, cortical, subcortical and deep perforated vessels were clearly distinguished. The penetration of the cortical arteries vertically into the cortex and terminating into different layers could be observed. Typical short, intermediate, long cortical and subcortical vessels were visible, which gave a clearer depiction of the complete spatial vascular network. The short vessels tended to be single, while the intermediate and long ones were clawed, fountain-like or willow-like. The subcortical artery in the cortex split over and over again, and the end branch entered subcortical white matter. The vascular network in the deep cerebral cortex tended to be more abundant than in superficial layers. Vessels in the medulla mostly exhibited corrugated or heliciform arrangements, supplying blood to deep functional areas. In particular, it was worth noting that a few of the larger cortical medullary arteries had no branches in the cortex, running directly in the cortex and wriggling in the medulla where the branches subsequently distributed in the form of a 'T'. Subcortical vessels mostly exhibited corrugated arrangements or heliciform, right-angled or forming substantial obtuse branches in the brain parenchyma. The cerebral vessel branches were extraordinarily numerous, and, as the vessel diameter decreased dramatically, the number of blood vessels significantly increased. These results demonstrated that the maintenance of the physiological function of the brain had a significant demand for oxygen and nutrients, and was closely related to the hierarchy and integrity of microcirculation. The intricate microvascular network distributed in the important functional brain areas and anastomosed with each other, which was likely to compensate for potential damage to a certain extent.

3.3. 3D pseudo-color rendering image of cerebral angioarchitecture

After phase retrieval and reconstruction, numerous cerebral microvasculature sketched a broad outline of the global network skeleton map [Fig. 3(A)]. The vascular network composite of blood vessels with variable diameters was

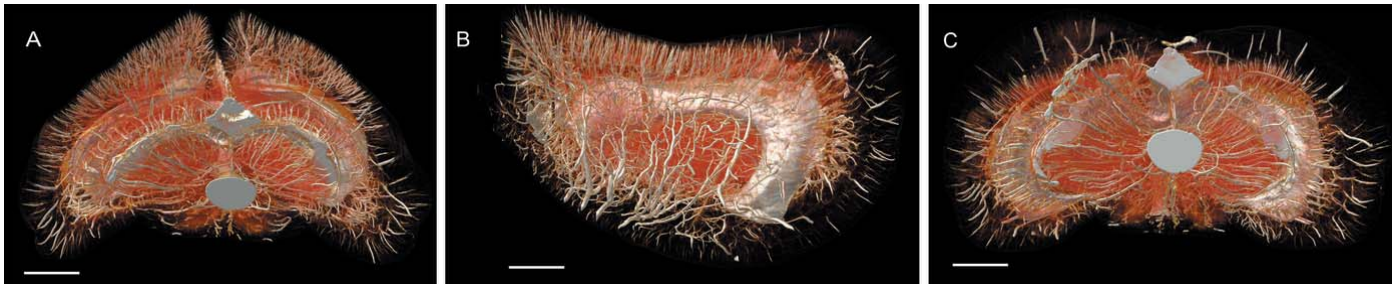

Figure 2
3D tomography of cerebral angioarchitecture in the three planes. Scale bars = 1 mm. (A) Top view. (B) Lateral view. (C) Antapical view.

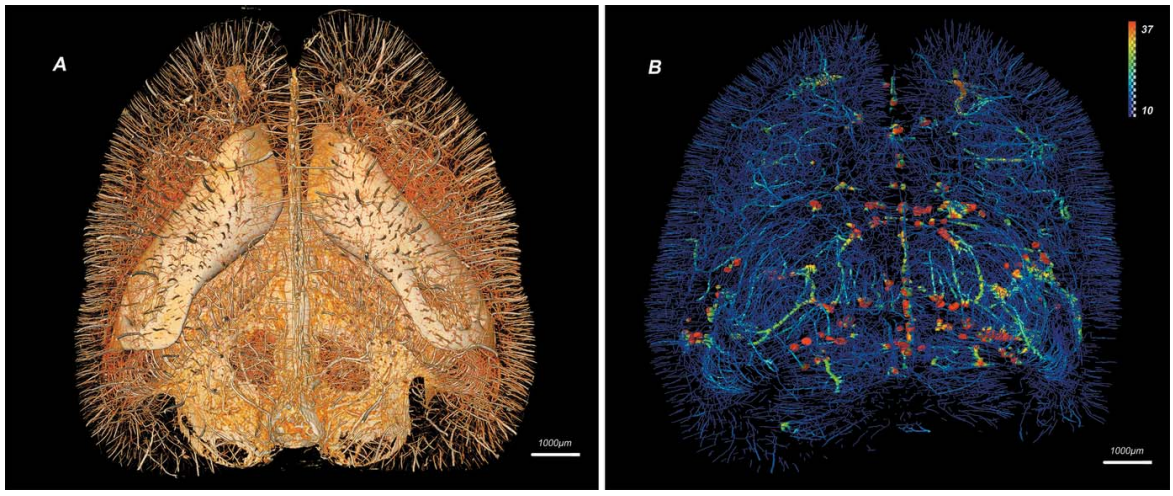

Figure 3
Extraction of the vascular network skeleton. (A) The segmented images were inverted to highlight the vessels. (B) Rendering of the 3D digitalized maps of vasculature. The color gradients reflect vessel diameters, ranging from 10 μm (blue) to 37 μm (red). Scale bars = 1 mm.

extracted and represented with pseudo-color for quantitative analysis. The image [Fig. 3(B)] demonstrated that microvessels in the blue region were arranged in a continuous and dense criss-cross pattern, which could not be manifested in a conventional CT scan.

3.4. Morphology of selected brain regions from 2D to 3D perspective in multi-angles

We selected functional brain regions (regions of interest, ROIs) that contain important structures such as the midbrain and corpus striatum, showing the spatial structure of blood vessels and the peripheral tissue in 2D virtual slices and providing abundant anatomical information. On this basis, further reconstruction was carried out to obtain 3D blood supply distribution in the ROIs (Fig. 4). With respect to architectonics, our work revealed the integrated microvascular connectivity of ROIs precisely via in-line PCI from multiple angles and different levels.

3.5. Comparison of HE staining and SR images of the brain

HE-stained sections of brains in mice [Fig. 5(A)] were compared with their corresponding reconstructive 3D virtual

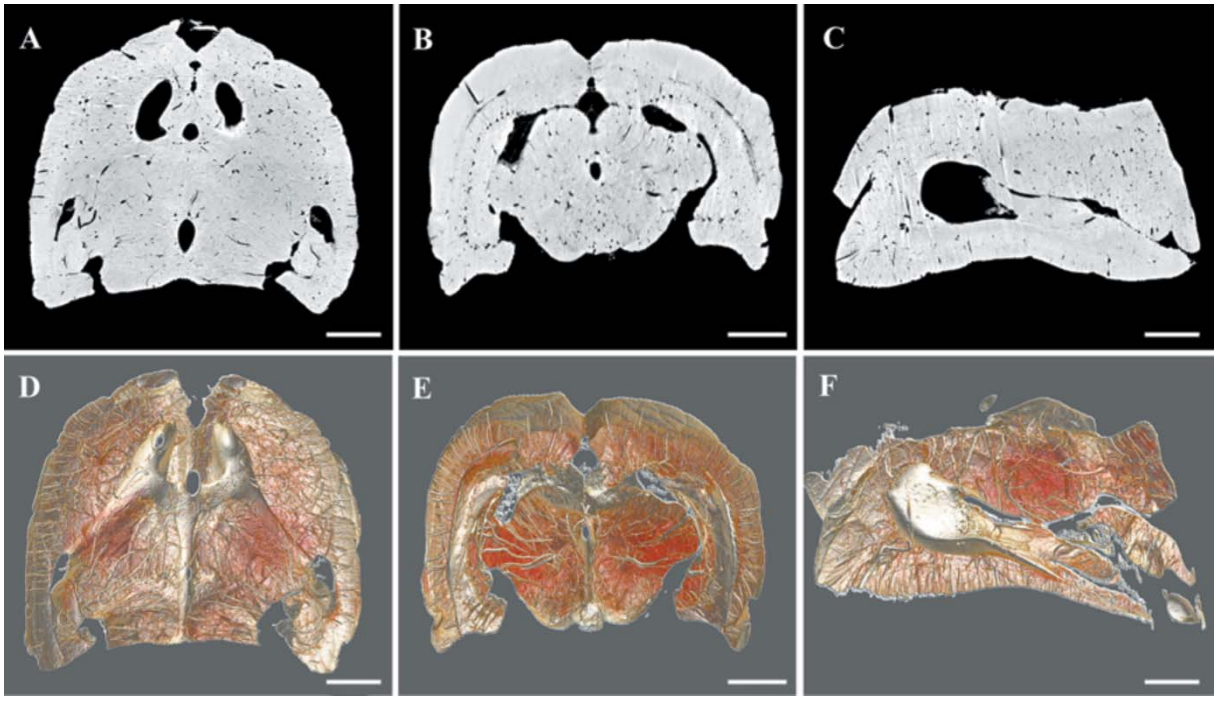

Figure 4
Digital anatomical images from 2D to 3D. (A)–(C) Multi-angle 2D virtual tissue sections. (D)–(F) Multi-angle 3D rendering corresponding images. Scale bars = 1 mm.

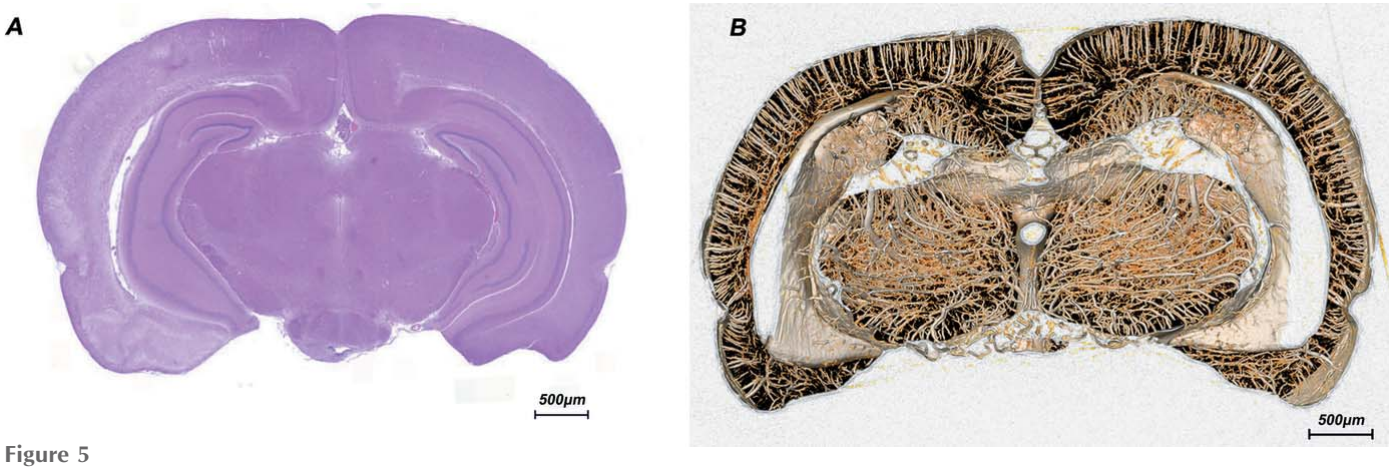

Figure 5
Representative HE staining slices compared with 3D images by SR phase contrast imaging. (A) Brain HE staining. (B) 3D corresponding reconstructive coronal virtual brain section. Scale bars = 500 μm.

brain sections [Fig. 5(B)]. The results of the 3D rendering images showed consistency with histological staining while the latter one sacrificed the integrity of the sample by sectioning for histological sample preparation requirement. In particular, the SR technique showed the ability to provide more detailed information of the complicated brain microstructure as well as microvascular distribution with coloring rendering of stereostructure.

3.6. 3D pseudo-color connectivity map of focal angioarchitecture compared with 2D CD31 immunohistochemistry

We have observed microvessels with widths as small as 10 μm, *i.e.* approximately the size of capillaries. The selected corresponding 2D virtual tissue sections could not depict the overall perspective of a typical vessel, whereas 3D rendering images could reflect the authenticity of the blood vessel morphology [Figs. 6(A)–6(C)]. To further confirm the accuracy of SR imaging, we obtained CD31 immunohistochemistry images at the corresponding brain region with a high-level magnification. The brown-staining particles located in the membrane of vascular endothelium represented CD31-positive microvessels, which depicted curved and tube-like blood vessels irregularly in the cross-section view [Fig. 6(D)]. The images showed consistency that microvessels approximately 10 μm wide could be discriminated in 2D histological sections as well as 3D SR imaging. Remarkably, the delicate vascular spatial structure of the brain was investigated in greater detail using the SR technique.

3.7. 3D virtual cerebrovascular micro-endoscopy

By virtue of 3D reconstruction, we attempted to perform virtual cerebrovascular micro-endoscopy on the basis of surface rendering (Fig. 7). The fundamental process included path planning and real-time rendering following the route settings of the camera. The pivotal issue was to simulate virtual camera recordings, while moving through a targeted vessel lumen dynamically. Concurrent application of 3D virtual flight through the brain space with high resolution was possible with automatic navigation through the vessel lumen losslessly, which was able to avoid microvascular injury with angiographic methods. This could be of great significance for

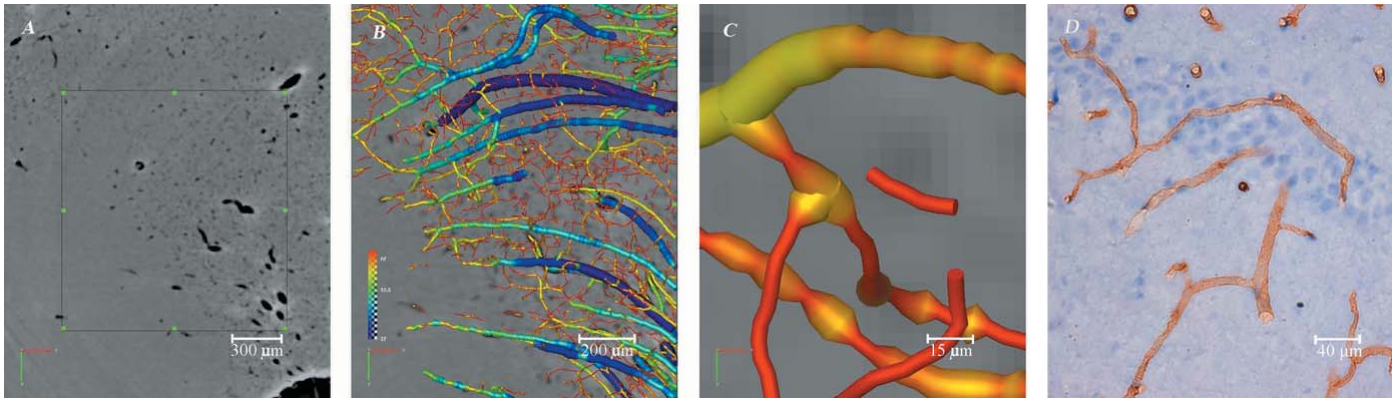

Figure 6
3D reconstruction of an ROI with a 3.7 μm detector. (A) 2D slice; the black frame represents the target reconstructed region. (B) 3D tomography of the local angioarchitecture (with the ROI denoted by the white frame). This area is shown with even higher magnification in (C). The color gradients reflect vessel diameters, ranging from 10 μm (red) to 37 μm (dark blue). (D) CD31 immunohistochemistry. Brown-staining particles represent the membrane of vascular endothelium which were stained by CD31 antibody.

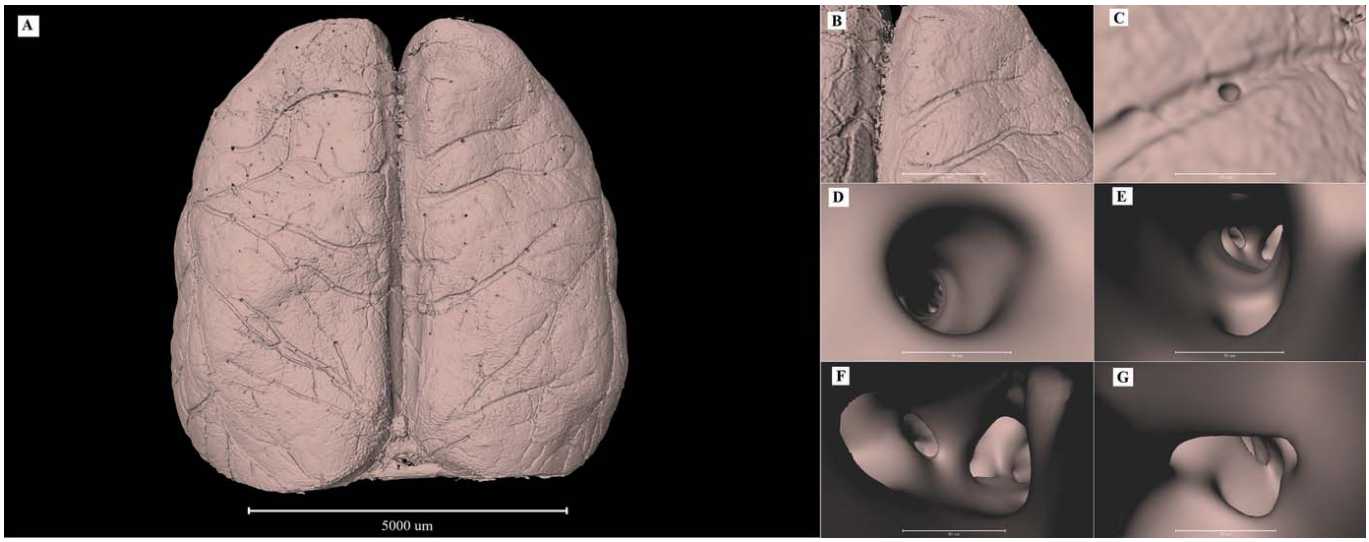

Figure 7
3D virtual micro-endoscopy for cerebral vessels. (A) Overall view of the brain. (B, C) Initiation to orientate the target cerebral vessel. (D)–(G) Successive vessel pathway tracing show the endovascular micro-structure of the inner surface of cerebral vessels. (A) Scale bar = 5000 μm. (B) Scale bar = 1000 μm. (C) Scale bar = 300 μm. (D, E) Scale bar = 90 μm. (F) Scale bar = 80 μm. (G) Scale bar = 70 μm.

stereoscopic visualization and measurement of endovascular anatomy under pathological conditions.

4. Discussion

The integrity and orderliness of cerebral vessels are the foundation for maintaining the function of the central nervous system (Stiles & Jernigan, 2010; Tata *et al.*, 2015). It is of vital importance for early diagnosis and treatment of cerebrovascular diseases to identify the morphological changes of the microvascular network (Cabrera DeBuc *et al.*, 2017; Park & Payne, 2016). In this study, the brain 3D microvascular images reconstructed by SR-based PPCI technology can clearly show the rich blood distribution in the inner cortex and other functional brain regions. Additionally, the results of 3D virtually reconstructive images largely match with findings on HE staining and CD31 immunohistochemistry, demonstrating the accuracy and reliability of the SR-based PPCI method and confirming that it can be used to identify the distribution of the vascular system and brain microstructure without angiography and sectioning.

From the perspective of stereology, we have described the spatial characteristics of cortical vessels and medullary vessels, providing important imaging evidence for elucidating the hemodynamics and significance of cerebrovascular microcirculation. Through the skeleton analysis of vascular network, we further find that the microvascular network in deep cortex and some important brain regions is densely distributed. The oxygen consumption of tissues in this area is relatively high, which is likely to be related to the number, size and metabolism of neurons from an anatomic point of view. The medullary vessels display an obtuse or right-angle shape, the majority of which are in a spiral or corrugated shape. These special morphologies can lead to changes of blood rheology, including blood flow turbulence or vortex. As a result, shear stress increases on the vascular endothelial cells and is prone to induce cell injuries, which may become a fundamental aspect of cerebral hemorrhage in the medulla.

Despite the rapid development of computer and imaging technology, more and more brain information has been obtained (Ashburner *et al.*, 2003; Bles & Haynes, 2008; Bromby, 2011). Nevertheless, *in situ* monitoring of microvessels below 10 μm is still the main barrier to the current medical imaging methods (Ashburner *et al.*, 2003; Bles & Haynes, 2008; Bromby, 2011; Upputuri *et al.*, 2015; Lugo-Hernandez *et al.*, 2017). The traditional imaging methods such as computed tomography angiography, magnetic resonance angiography and digital subtraction angiography illustrate the main arteries, failing to track the pathways of the microvascular network (Beck & Plate, 2009; Yanev & Dijkhuizen, 2012). In recent years, increasing applications of microcomputed tomography (μCT) have greatly improved the spatial resolution of images. It holds the advantages of intact sample preservation without requirement for serial histological sectioning and can be used to obtain microstructure of detached microvessels (Cao *et al.*, 2015; Zagorchev *et al.*, 2010). Heinzer *et al.* (2006) and Heinzer (2008) have managed hierarchical visualization of brain vascular network utilizing μCT, SRμCT and scanning electron miscroscopy, and they use the vascular corrosion casting (VCC) method via a synthetic polymer filling the vessel lumens with dispelling of the peripheral brain parenchyma. These techniques depend on the filling states of the contrast agents in vessels and appropriate perfusion pressure; therefore it is difficult to obtain comprehensive and reliable 3D vascular networks on account of potential risks (Zagorchev *et al.*, 2010; Vasquez *et al.*, 2011; Tse *et al.*, 2017), for instance, leakage of contrast agents under excessively high perfusion pressure or incomplete filling of agents in small vessels, especially in brain capillaries with lower pressure (Zhang *et al.*, 2015). Any defects during these

processes will lead to inaccurate vascular imaging. With relatively easier and non-invasive preparation procedures, we have preserved the cerebral microvascular network with striking phase contrast.

As a rule, ordinal experimental steps such as perfusion with paraformaldehyde, contrast agent injection, fixation and dehydration are incorporated in *ex vivo* procedures of brain sample preparation for current μCT or SRμCT scanning. In fact, especially for the last dehydration step, scanning requires the samples to be fully dried, given that this may probably induce a certain degree of deformation of tissues. Although this unavoidably affects the 3D visualization of brain angioarchitecture *ex vivo*, previous research has verified that the extent of deformation is within an acceptable range by the current methods (Huang *et al.*, 2015; Lin *et al.*, 2015; Zysk *et al.*, 2012). As a matter of fact, it is reasonable to use air as a contrast agent in PPCI which captures the phase contrast through refractive index gradients. The blood-filling samples fixed in formalin, especially when prepared in phosphate buffered saline (PBS), are proposed to be in a status in closer proximity to the normal physiological conditions without any additional contrast agent. Thus the primary morphological patterns are theoretically better maintained than when using other more invasive processing methods. Hence, we are now attempting to apply an alternative tissue fixation medium closer to *in vivo* states, aiming to decrease potential structural changes in the dehydration procedure. Furthermore, the VCC method uses special chemical reagents to eliminate the brain parenchyma with only the preservation of the vascular skeleton. In comparison, we are able to keep the brain relatively intact, which is more favorable for presenting anatomical morphological relationships between vasculature and surrounding parenchyma. We can further extract the reserved vascular framework alone without the aid of contrast agents or the VCC method. In our ongoing study in ischemic stroke and cerebral hemorrhage models, we use PPCI to observe the structural changes of the lesion region and following remodeling of the vascular network, without processing complications such as leakage of contrast agents and incomplete filling of the vessel lumens.

Synchrotron radiation light sources have unique properties, including high collimation, high polarization, high purity and high brightness, high stability, high throughput, quasi-coherence, and especially high spatial resolution, which is an incomparable advantage of the SR light source compared with the conventional X-ray film (Zhang *et al.*, 2014*a*; Chen *et al.*, 2014). Remarkably, PPCI based on SR avoids the invasive sections compared with the histological procedure. It predigests the imaging process without the aid of the destructive vessel casting perfusion technique. The PPCI images in our present study provide multiple perspectives for brain angioarchitectural structure from the 2D virtual sections to 3D configurations. With respect to the mouse brain, the entire *ex vivo* regions, including focal vascular connectivity, have been vividly presented for the first time in a detailed 3D morphology. Here, in order to gain further insight into the vessel characteristics of the brain, local vessel branches are automatically labeled with its anatomical features with unique color. Compared with histological sections, the SR-PPCI technique, with its advantage of high resolution, has proven to be a reliable tool to visualize microvessels on the micrometer scale. In addition, SR-PPCI does not need ultramicrotomy, thus avoiding destruction of the whole brain and loss of information.

Virtual endoscopy has been applied in various systems (Bartz, 2005) such as the heart (Herzog *et al.*, 2001; Xue *et al.*, 2010; Yao *et al.*, 2018) and spinal canal (Kotani *et al.*, 2012). With the aid of a 3D navigation system, the position and orientation of the inner profile of the vessel can be 'real time' exploited and tracked with a series of 3D digitalized image. The 3D virtual endoscopy models allow for deep insight understanding the nature and role of these intricate microstructures (Sun & Lawrence, 2009).

However, the PPCI technique has a few limitations. A large sample volume can only be acquired with low resolution and magnification, owing to its large field of view. In this study, we intend to establish 3D imaging of brain-wide vasculature at the cost of resolution loss. Although using detectors with higher resolution may solve this problem to some extent (Zhang *et al.*, 2015), how to broaden the field of view with higher resolution remains challenging. Moreover, a longer preparation time for sample dehydration and fixation is needed for larger samples. Particular attention should be devoted to the optimization of imaging conditions to image with higher resolution and lower radiation dose, and *in vivo* 4D dynamic imaging is needed. In summary, the presented method is promising in a broad range of life science applications, such as 3D printing (Irsen *et al.*, 2007; Ryu *et al.*, 2018), tissue engineering (Peyrin *et al.*, 2007; Papadimitropoulos *et al.*, 2008; Olubamiji *et al.*, 2014), blood flow simulation (Adam *et al.*, 2003; Goldston *et al.*, 2005), drug discovery (Wallace & Janes, 2003; Wasserman *et al.*, 2012), even in combination with SR microbeam X-ray fluorescence or SR-based Fourier transform infrared microspectroscopy for in depth analysis.

Our present study provides valuable hierarchical imaging of angioarchitecture at ultra-high resolution using SR-based PPCI techniques to elucidate the underlying mechanism of vascular hemodynamics of brain. Currently, SR-based PPCI is a powerful tool used in experimental studies to identify pathological changes. Therefore, we hold the prospect of using this technique to perform more in-depth studies of morphological analysis of neurovascular alterations and evaluation of therapeutic strategies in various diseases.

Acknowledgements

This program was completed at the BL13W beamline of the Shanghai Synchrotron Radiation Facility (SSRF) in China. The authors would like to thank the staff at the BL13W station of SSRF for their kind guidance during the experiments. We thank Professor Xianzhen Yin for his assistance in image processing. The authors declare that the research was conducted in the absence of any commercial or financial relationships that could be construed as a potential conflict of interest.

Funding information

The following funding is acknowledged: National Natural Science Foundation of China (grant Nos. 81501025 and 81601094); Natural Science Foundation of Hunan Province (grant No. 2016JJ3174); Science Foundation of Xiangya Hospital for Young Scholar (grant No. 2017Q01).

References

Adam, J. F., Elleaume, H., Le Duc, G., Corde, S., Charvet, A. M., Troprès, I., Le Bas, J. F. & Estève, F. (2003). *J. Cereb. Blood Flow Metab.* **23**, 499–512.
Ashburner, J., Csernansky, J. G., Davatzikos, C., Fox, N. C., Frisoni, G. B. & Thompson, P. M. (2003). *Lancet Neurol.* **2**, 79–88.
Bartz, D. (2005). *Comput. Graph. Forum*, **24**, 111–126.
Beck, H. & Plate, K. H. (2009). *Acta Neuropathol.* **117**, 481–496.
Bles, M. & Haynes, J. D. (2008). *Neurocase*, **14**, 82–92.
Bravin, A., Coan, P. & Suortti, P. (2013). *Phys. Med. Biol.* **58**, R1–R35.
Bromby, M. (2011). *Cortex*, **47**, 1261–1262.
Bukreeva, I., Campi, G., Fratini, M., Spano, R., Bucci, D., Battaglia, G., Giove, F., Bravin, A., Uccelli, A., Venturi, C., Mastrogiacomo, M. & Cedola, A. & Bukreeva, I. (2017). *Sci. Rep.* **7**, 41054.
Cabrera DeBuc, D., Somfai, G. M. & Koller, A. (2017). *Am. J. Physiol. Heart Circ. Physiol.* **312**, H201–H212.
Cao, Y., Wu, T., Yuan, Z., Li, D., Ni, S., Hu, J. & Lu, H. (2015). *Sci. Rep.* **5**, 12643.
Carlton, H. D., Elmer, J. W., Li, Y., Pacheco, M., Goyal, D., Parkinson, D. Y. & MacDowell, A. A. (2016). *J. Vis. Exp.* **110**, e53683.
Cedola, A., Bravin, A., Bukreeva, I., Fratini, M., Pacureanu, A., Mittone, A., Massimi, L., Cloetens, P., Coan, P., Campi, G., Spanò, R., Brun, F., Grigoryev, V., Petrosino, C., Venturi, C., Mastrogiacomo, M., Kerlero de Rosbo, N. & Uccelli, A. (2017). *Sci. Rep.* **7**, 5890.
Chen, R., Liu, P., Xiao, T. & Xu, L. X. (2014). *Adv. Mater.* **26**, 7688–7691.
Chen, R.-C., Dreossi, D., Mancini, L., Menk, R., Rigon, L., Xiao, T.-Q. & Longo, R. (2012). *J. Synchrotron Rad.* **19**, 836–845.
Fratini, M., Bukreeva, I., Campi, G., Brun, F., Tromba, G., Modregger, P., Bucci, D., Battaglia, G., Spanò, R., Mastrogiacomo, M., Requardt, H., Giove, F., Bravin, A. & Cedola, A. (2015). *Sci. Rep.* **5**, 8514.
Giuliani, A., Mazzoni, S., Mele, L., Liccardo, D., Tromba, G. & Langer, M. (2017). *Front. Physiol.* **8**, 769.
Goldston, J. E., Quataert, E. & Igumenshchev, I. V. (2005). *Astrophys. J.* **621**, 785–792.
Heinke, J., Patterson, C. & Moser, M. (2012). *Front. Biosci. Elite Ed.* E**4**, 2269–2288.
Heinzer, S. (2008). *NeuroImage*, **39**, 1549–1558.
Heinzer, S., Krucker, T., Stampanoni, M., Abela, R., Meyer, E. P., Schuler, A., Schneider, P. & Muller, R. (2006). *NeuroImage*, **32**, 626–636.
Herzog, C., Ay, M., Engelmann, K., Abolmaali, N., Dogani, S., Diebold, T. & Vogl, T. J. (2001). *Rofo Fortschr. Geb. Rontgenstr. Neuen Bildgeb. Verfahr.* **173**, 341–349.
Hu, J., Cao, Y., Wu, T., Li, D. & Lu, H. (2014). *Med. Phys.* **41**, 101904.
Hu, J., Cao, Y., Wu, T., Li, D. & Lu, H. (2015). *Spinal Cord*, **53**, 585–590.
Hu, J., Ni, S., Cao, Y., Wang, X., Liao, S. & Lu, H. (2017). *Spine*, **42**, E883–E889.
Huang, S., Kou, B., Chi, Y., Xi, Y., Cao, Y., Cui, W., Hu, X., Shao, Z., Guo, H., Fu, Y., Xiao, T., Sun, J., Zhao, J., Wang, Y. & Wu, J. (2015). *Sci. Rep.* **5**, 9418.
Irsen, S., Leukers, B., Tille, C., Beckmann, F., Müller, B., Buzug, T. & Seitz, H. (2007). *Advances in Medical Engineering*, pp. 121–126. Springer.
Kline, T. L., Zamir, M. & Ritman, E. L. (2010). *Ann. Biomed. Eng.* **38**, 2851–2864.
Kotani, T., Nagaya, S., Sonoda, M., Akazawa, T., Lumawig, J. M., Nemoto, T., Koshi, T., Kamiya, K., Hirosawa, N. & Minami, S. (2012). *Spine*, **37**, E752–E756.
Lazzari, M. & Franceschini, V. (2000). *J. Anat.* **197**(Pt 2), 167–175.
Liao, S., Ni, S., Cao, Y., Yin, X., Wu, T., Lu, H., Hu, J., Wu, H. & Lang, Y. (2017). *J. Synchrotron Rad.* **24**, 1218–1225.
Lin, H., Kou, B., Li, X., Wang, Y., Ding, B., Shi, C., Liu, H., Tang, R., Sun, J., Yan, F. & Zhang, H. (2015). *PLoS One*, **10**, e0121438.
Lindvere, L., Dorr, A. & Stefanovic, B. (2010). *Cold Spring Harb Protoc.* **2010**, doi:10.1101/pdb.prot5494.
Lorenzo, M., Inna, B. & Giulia, S. (2019). *NeuroImage*, **184**, 490–495.
Lugo-Hernandez, E., Squire, A., Hagemann, N., Brenzel, A., Sardari, M., Schlechter, J., Sanchez-Mendoza, E. H., Gunzer, M., Faissner, A. & Hermann, D. M. (2017). *J. Cereb. Blood Flow Metab.* **37**, 3355–3367.
Mazzetti, S., Librizzi, L., Frigerio, S., de Curtis, M. & Vitellaro-Zuccarello, L. (2004). *Brain Res.* **999**, 81–90.
Olubamiji, A. D., Izadifar, Z. & Chen, D. X. (2014). *Tissue Eng. B*, **20**, 503–522.
Paganin, D., Mayo, S. C., Gureyev, T. E., Miller, P. R. & Wilkins, S. W. (2002). *J. Microsc.* **206**, 33–40.
Papadimitropoulos, A., Friess, S., Beckmann, F., Salmon, P., Riboldi, S., Hutmacher, D., Martin, I. & Müller, B. (2008). *Proc. SPIE*, **7078**, 70780T.
Park, C. S. & Payne, S. J. (2016). *Med. Eng. Phys.* **38**, 41–47.
Peyrin, F., Mastrogiacomo, M., Cancedda, R. & Martinetti, R. (2007). *Biotechnol. Bioeng.* **97**, 638–648.
Ryu, M., Linklater, D., Hart, W., Balčytis, A., Skliutas, E., Malinauskas, M., Appadoo, D., Tan, Y. E., Ivanova, E. P., Morikawa, J. & Juodkazis, S. (2018). *J. Opt.* **20**, 035101.
Solis, E. Jr, Afzal, A. & Kiyatkin, E. A. (2018). *Neuropharmacology*, **133**, 481–490.
Stiles, J. & Jernigan, T. L. (2010). *Neuropsychol. Rev.* **20**, 327–348.
Sun, Z. & Lawrence, B. (2009). *Biomed. Imaging Intervent. J.* **5**, e22.
Tata, M., Ruhrberg, C. & Fantin, A. (2015). *Mech. Dev.* **138**, 26–36.
Tse, J. J., Dunmore-Buyze, P. J., Drangova, M. & Holdsworth, D. W. (2017). *Contrast Media Mol. Imaging*, **2017**, 7368384.
Upputuri, P. K., Sivasubramanian, K., Mark, C. S. & Pramanik, M. (2015). *Biomed. Res. Int.* **2015**, 783983.
Vasquez, S. X., Gao, F., Su, F., Grijalva, V., Pope, J., Martin, B., Stinstra, J., Masner, M., Shah, N., Weinstein, D. M., Farias-Eisner, R. & Reddy, S. T. (2011). *PLoS One*, **6**, e19099.
Wallace, B. A. & Janes, R. W. (2003). *Biochem. Soc. Trans.* **31**, 631–633.
Wasserman, S. R., Koss, J. W., Sojitra, S. T., Morisco, L. L. & Burley, S. K. (2012). *Trends Pharmacol. Sci.* **33**, 261–267.
Wu, T., Cao, Y., Ni, S., Luo, Z., Jiang, L., Lu, H. & Hu, J. (2018). *Spine*, **43**, E504–E511.
Xue, H., Sun, K., Yu, J., Chen, B., Chen, G., Hong, W., Yao, L. & Wu, L. (2010). *Int. J. Cardiovasc. Imaging*, **26**, 851–859.
Yanev, P. & Dijkhuizen, R. M. (2012). *Stroke*, **43**, 3436–3441.
Yao, L. P., Mei, J., Ding, F. B., Zhang, L., Li, H. M., Ding, M., Yang, X., Li, X. M. & Sun, K. (2018). *Sci. Rep.* **8**, 1424.
Zagorchev, L., Oses, P., Zhuang, Z. W., Moodie, K., Mulligan-Kehoe, M. J., Simons, M. & Couffinhal, T. (2010). *J. Angiogen. Res.* **2**, 7.
Zhang, M., Peng, G., Sun, D., Xie, Y., Xia, J., Long, H., Hu, K. & Xiao, B. (2014*a*). *Med. Phys.* **41**, 031907.
Zhang, M.., Sun, D. N., Xie, Y. Y., Peng, G. Y., Xia, J., Long, H. Y. & Xiao, B. (2014*b*). *Br. J. Radiol.* **87**, 20130670.
Zhang, M., Zhou, L., Deng, Q. F., Xie, Y. Y., Xiao, T. Q., Cao, Y. Z., Zhang, J. W., Chen, X. M., Yin, X. Z. & Xiao, B. (2015). *Sci. Rep.* **5**, 14982.
Zhou, S. A. & Brahme, A. (2008). *Phys. Med.* **24**, 129–148.
Zysk, A. M., Garson, A. B., Xu, Q., Brey, E. M., Zhou, W., Brankov, J. G., Wernick, M. N., Kuszak, J. R. & Anastasio, M. A. (2012). *Biomed. Opt. Expr.* **3**, 1924.